Chiral nematic droplets with parallel surface anchoring

F. Xu and P. P. Crooker
Department of Physics and Astronomy, University of Hawaii, Honolulu, Hawaii 96822
(Received 26 June 1997)

Chiral nematic droplets of various radii R and intrinsic pitch P with parallel boundary conditions have been observed using a polarizing microscope. The visual appearances of the droplets have been compared with computer simulations from model director fields. It is found that the director configuration depends strongly on the ratio R/P. For $P>R$, the droplets have a twisted bipolar structure. For $P<R$, the director field takes on the Frank-Pryce structure. For $P \ll R$, the droplet appearance is similar to that of a radial nematic drop, but the director field is still described by the Frank-Pryce model. We present a phase stability diagram for the two structures, and show how the structural transition between them proceeds continuously through intermediate states. [S1063-651X(97)09312-4]

PACS number(s): 61.30.Gd, 61.30.Jf

I. INTRODUCTION

Liquid crystals confined in restricted geometries have been intensively studied in recent years. [1–3] This interest has been both scientific and technological. Scientifically, confinement produces unusual textures and defects due to the topological incompatibility between the bulk and surface alignment of the liquid crystal molecules. In addition, confinement may also modify the phase transitions of some liquid crystal systems. When parameters such as temperature, external field, chirality, and the elastic constants of a confined liquid crystal change, unusual structural and thermodynamic phase transitions occur which do not occur in the bulk.

Technologically, surface alignment and texture formation are always the most important factors in any application of liquid crystals. In twisted nematic or super twisted nematic displays, liquid crystals are confined between aligning planar surfaces to achieve a texture useful for electro-optical effects. In polymer-dispersed liquid crystal displays, micrometer-sized nematic droplets with aligning surfaces are used for light switching [4]. In both cases, the confining surface provides a characteristic texture alignment of the liquid crystal, and an electric field transforms that texture to another texture with different optical properties.

In this paper we are concerned with liquid crystals in droplets. The main structures of *nematic* droplets have been identified [5–9], transitions between those structures have been studied [10], and several techniques for structure determination have now become well established [5,10]. More recently, confined *chiral nematic* liquid crystal systems have become interesting because of their very unusual structures and defects [11,12]. Understanding chiral nematic structures is also of practical importance, because chiral nematic droplets have been used to develop color displays [13].

Because of their intrinsic chirality, structures of chiral nematic systems are more complicated than those of nematics. Although some structures of chiral nematic droplets and cylinders have been found experimentally, the relations between those structures and the controlling parameters—elastic constants, temperature, surface anchoring strength, external field, or intrinsic chirality—are hardly known. Recent theoretical studies on chiral nematic droplets by Zumer and co-workers [14,15] provided a good understanding of these systems, although some of their derived results are yet to be tested.

This paper presents an experimental study of the behavior of chiral nematic droplets with parallel boundary conditions as the chirality and droplet size are changed. Our technique consists of recording images of the drops using polarized microscopy, and comparing them to simulated images calcu-

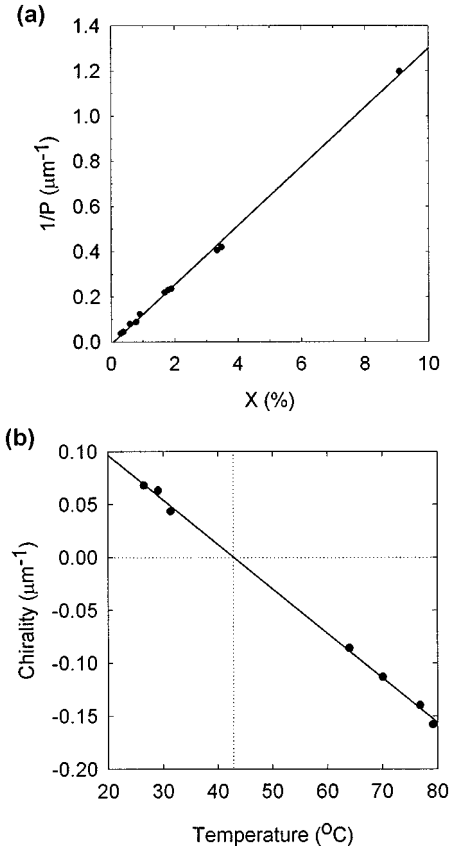

FIG. 1. (a) Chirality $1/P$ of the ZLI-4788-000–S-811 mixture vs concentration X of S-811. (b) Chirality of the ZLI-2806–D-112–D-13 mixture vs temperature.

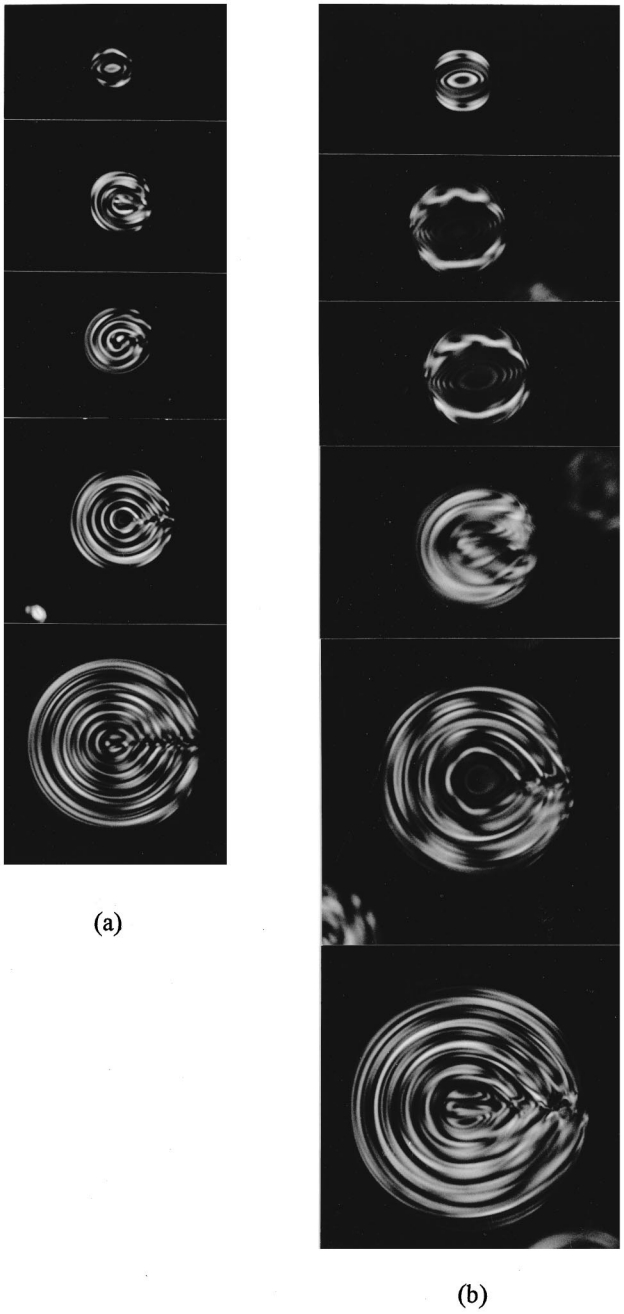

FIG. 2. Evolution of texture with pitch P. (a) $P=7.4\ \mu$m and $R=8.2$, 10.3, 13.0, 18.9, and 31.4 μm from top to bottom; (b) $P=17.7\ \mu$m and $R=11.5$, 17.7, 19.5, 22.5, 34.8, and 41.0 μm from top to bottom.

lated from proposed director fields. From this comparison we are able to determine the director field and how it depends on chirality. We also describe a mechanism which shows how the transition between two topologically different structures can take place continuously.

II. EXPERIMENT

Two different liquid crystal mixtures were used in this study. To study the droplet structures in stable configurations we used mixtures of ZLI-4788-000 (a propriety nematic from E. Merck) and a chiral dopant S-811 (E. Merck). The

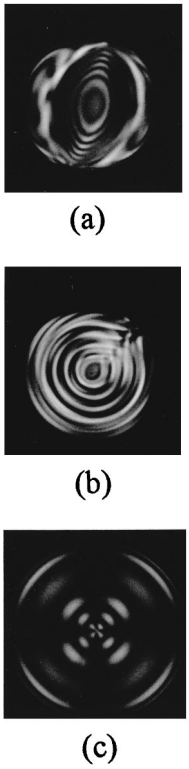

FIG. 3. Examples of drops with (a) low chirality $P>R$, (b) high chirality $P<R$, and (c) very high chirality $P\ll R$.

chirality $q=1/P$ (where P is the pitch) of the mixture is proportional to the concentration of S-811 as shown in Fig. 1.

To study the evolution of the structural transition with continuously changing chirality, we used a mixture of ZLI-2806 (a proprietary nematic mixture from E. Merck), and D-112 and D-13 (chiral dopants synthesized at Technical University Berlin [16]) in the weight percent ratio of 96.80:0.35:2.85, respectively. The chirality of this mixture is linear with temperature, also shown in Fig. 1.

Chiral nematic droplets were obtained by dispersing the chiralized liquid crystal into a polymer matrix made of equal weights of polyethylene glycol and polyvinyl-pyrrolidone(Aldrich Chemical). The matrix components were mixed at 150 °C, then the liquid crystal was added to form isotropic droplets. The dispersion was then sandwiched between glass slides separated by 150-μm spacers, and cooled to room temperature. The high viscosity of the polymer at room temperature (due to the polyvinyl-pyrrolidone) prevented the liquid crystal droplets from floating to the sample boundaries. Both liquid crystal mixtures possess parallel molecular anchoring at the polymer boundary.

Visually the droplets appeared spherical, as can be expected for a surrounding liquid matrix, and there was no observable tendency for the director field to drive the droplet shape away from that of a sphere. Droplet diameters ranged from less than 1 μm to over 100 μm. A polarizing microscope (Zeiss Universal) was used to measure the diameters of the droplets and to observe their transmission patterns. The sample was placed between crossed polarizers, illuminated monochromatically by a sodium lamp ($\lambda=589$ nm), and either visually observed, photographed, or recorded on

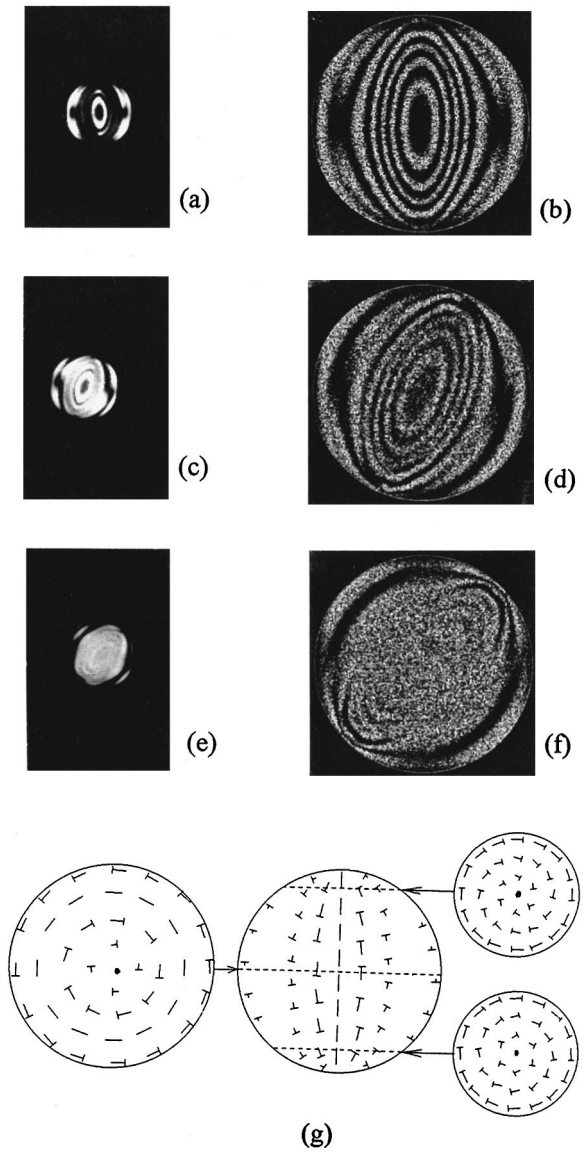

FIG. 4. A chiral nematic drop with $P>R$. Left column: droplet axis (a) parallel to polarizer, (c) at 22.5° to polarizer, and (e) at 45° to polarizer. Right column: computer-simulated transmission patterns of corresponding photographs in left column. (g) Director configuration used to calculate simulations.

video tape. The pitch of the liquid crystal mixtures was separately measured using the Cano ring technique [17].

III. RESULTS AND DISCUSSION

The director field of a chiral nematic liquid crystal droplet depends strongly on the radius R of the droplet and the pitch P of the liquid crystal. Other factors which may affect the structure are the elastic constant ratios, the surface anchoring strength, and the dielectric (or magnetic) anisotropy when an external field is applied. In this paper we only study the effects of size and pitch, leaving the effects of other parameters for future work.

In Fig. 2, we show images of droplets of ZLI-4788-000 and S-811 as seen under the polarizing microscope. In Fig. 2(a), $P=7.4$ μm, and the radii vary from 8.2 to 31.4 μm. In Fig. 2(b), $P=17.7$ μm, and the radii of the droplets varies

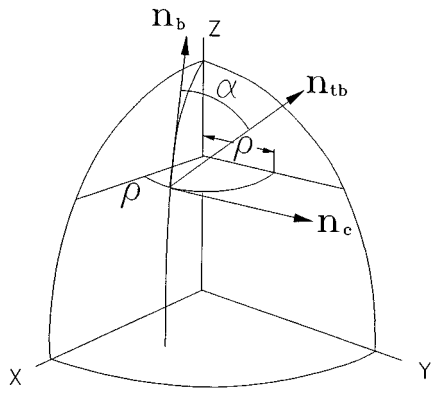

FIG. 5. Coordinates for twisted bipolar director field.

from 11.5 to 41.0 μm. There are three regimes, which we show in Fig. 3. For low chirality ($P>R$), we will show that the structure is twisted bipolar. For high chirality ($P<R$), the structure is the radial defect or Frank-Pryce structure. The third regime occur when $P \ll R$; although the appearance is much different, the structure is still Frank-Pryce. These regimes are discussed in more detail in the next few subsections.

A. Low chirality ($P>R$)

For low chirality ($P>R$), Bezic and Zumer (BZ) [14] predicted a bipolar structure in which the directors lie wholly in meridional planes. Our low-chirality droplets do not, however, exhibit the characteristic bipolar transmission pattern. When a low-chirality droplet is viewed with its axis perpendicular to the light and parallel to one of the polarizers (Fig. 4), the transmission pattern shows elliptical rings with the long axis parallel to the droplet axis and two dark regions near the edge on a line perpendicular to the droplet axis. As the droplet axis is rotated about the viewing direction, the dark regions evolve into an offset dark ring (shown at 22.5°), and finally a symmetrical dark ring at 45°.

These features do not match the features previously reported for bipolar droplets [5,9], but are similar to our previous results for nonchiral nematic droplets with a twisted bipolar director configuration [9]. We therefore propose a variation on the twisted bipolar model. Let $\mathbf{n}_b$ represent a bipolar director field, where the directors lie in the meridional plane, and let $\mathbf{n}_c$ represent a concentric field, where the directors lie in circles parallel to the equatorial plane and concentric with the droplet axis. $\mathbf{n}_{\rm tb}$ is the twisted bipolar director field according to

$$\mathbf{n}_{\rm tb}=\mathbf{n}_b\cos\alpha+\mathbf{n}_c\sin\alpha \tag{1}$$

where α is the angle between $\mathbf{n}_b$ and $\mathbf{n}_{\rm tb}$ (Fig. 5). Since the liquid crystal possesses intrinsic twist, our model assumes that α, expressed in cylindrical coordinates (ρ,ϕ,z), takes the form $\alpha=\alpha_0\rho/\rho_0$, where ρ_0 is the maximum radius of the $\rho-\phi$ cross section at z, and α_0 is the maximum twist angle at ρ_0. Here we are not trying to give a completely precise description of the director field; our goal is rather to obtain reasonable agreement between simulations and photographs in order to reveal the main topological features of the direc-

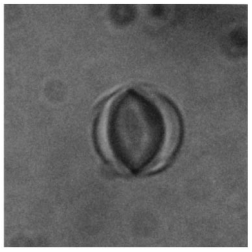

FIG. 6. A twisted bipolar droplet viewed without polarizers. Note the two refraction lines.

tor field. From this model we then calculate the optical transmission pattern, and compare the result with the experimental picture (Fig. 4).

This model differs from that for nematic twisted bipolar droplets in that the chiral nematic droplet has more twist than the nematic droplet. The amount of twist is revealed by the two refractive lines in Fig. 6. When the director rotates more than 90° between the axis and the surface, there is a locus of points where the director is parallel to the light ray and the refractive index ''seen'' by the ray is a minimum. As usual, the light refracts away from this minimum, and the regions appear dark.

Chiral nematic droplets also differ from nematic droplets in the radial dependence of the twist, as revealed by the behavior of $\alpha(\rho)$. For nematic droplets, the twist is not intrinsic, and α decays exponentially with ρ. For chiral nematic droplets, however, the twist is intrinsic, and $\alpha(\rho)$ is linear.

B. High chirality ($P<R$)

BZ [14] analyzed three director fields for high-chirality droplets ($P<R$). The radial defect or Frank-Pryce structure has an $s=2$ line defect along a radius; the diametrical defect structure has an $s=1$ line defect along a diameter; and the double radial defect structure has $s=\frac{1}{2}$ and $\frac{3}{2}$ line defects along each half of a diameter. From a free energy calculation they predicted that the diametrical defect structure is the most stable. It is interesting to compare these predictions to our observations (Fig. 7).

Our high-chirality droplets appear in two manifestations: either as a concentric ring pattern with a radial disclination

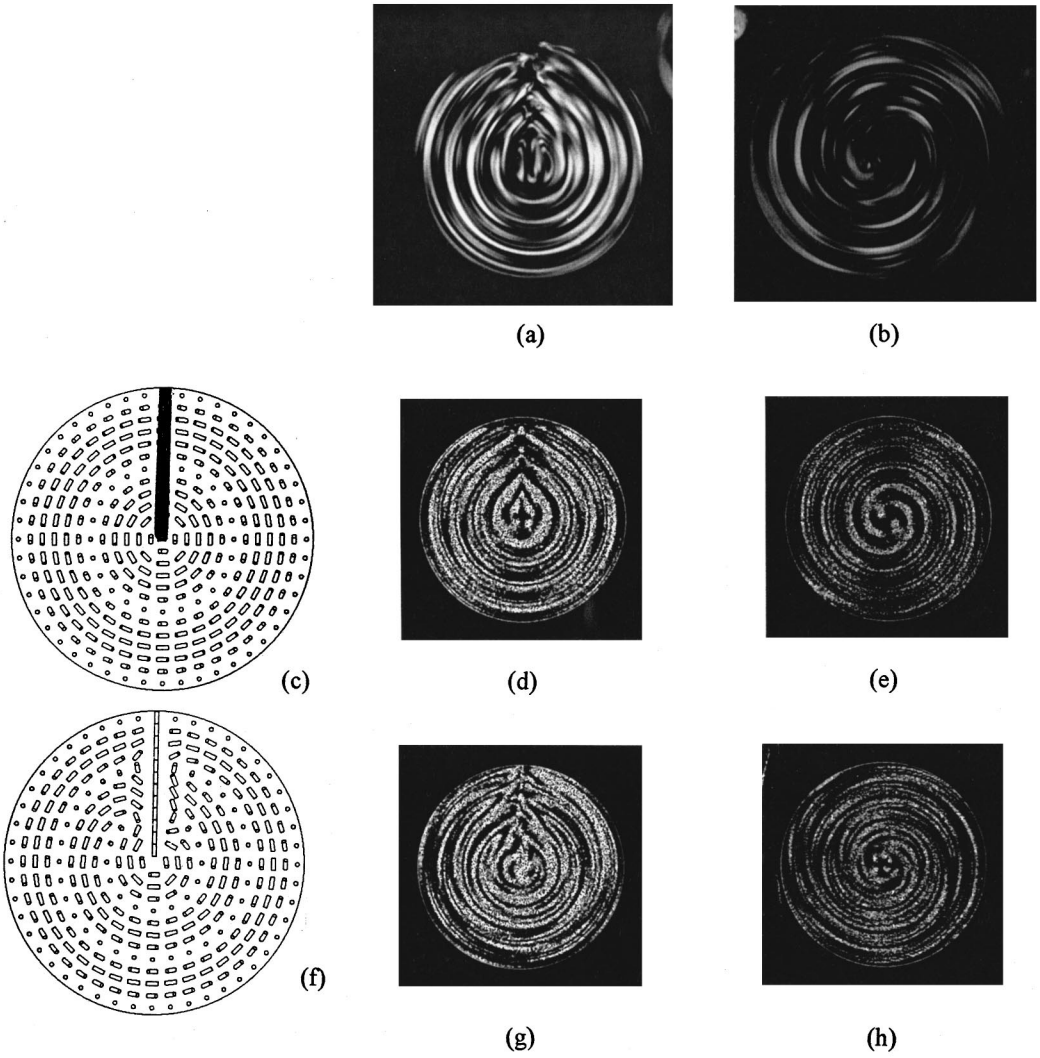

FIG. 7. Pictures of chiral nematic droplets with $P<R$ between crossed polarizers. (a) Disclination line parallel to polarizer; (b) disclination line parallel to light beam; (c) Frank-Pryce model with unescaped $\chi=2$ line; (d) and (e) simulation of (a) and (b) from model in (c); (f) escaped Frank-Pryce model with escaped $\chi=2$ line; (g) and (h) simulation of (a) and (b) from the model in (f).

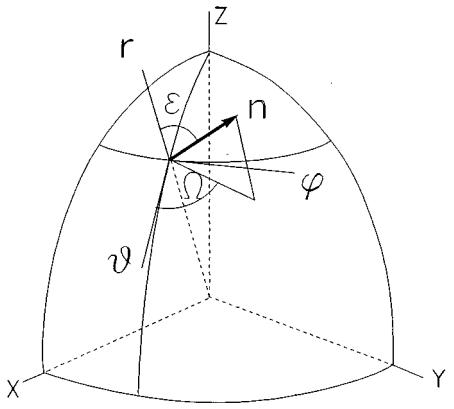

FIG. 8. Coordinates for the unescaped and escaped Frank-Pryce model.

[Fig. 7(a)], or as a spiral pattern with no disclination [Fig. 7(b)]. The former is characteristic of the Frank-Pryce structure when viewed perpendicular to the disclination line, while the latter is the same structure viewed along the disclination line. Figure 7(c) shows a cross section of the Frank-Pryce model in which the radial defect, a $\chi=2$ line, lies on the vertical radius from the center to the top. Optical simulations of Frank-Pryce droplets have been previously reported by Kitzerow and Crooker [18].

Since the $\chi=2$ defect line is topologically unstable, it can be converted to a nonsingular line by escaping the director in the radial direction as shown in Fig. 7(f). In order to determine whether the observed disclination line is singular or nonsingular, we show simulations from both the original (singular) Frank-Pryce model and the escaped (nonsingular) Frank-Pryce model, and compare the results with the microscope photographs of the droplets.

The original Frank-Pryce model is described by the director components in spherical coordinates,

$$(n_r, n_\theta, n_\phi) = (0, \cos\Omega, \sin\Omega), \tag{2}$$

where

$$\Omega = \phi + qr + \Omega_0 \tag{3}$$

is the angle between the director and a meridional line (Fig. 8). Here $q=2\pi/P$, and Ω is a constant. The transmission patterns calculated from this model [Figs. 7(d) and 7(e)] simulate the rings in the data well, except for the region near the disclination line. Note that the observed rings are offset across the disclination line; in the simulation, the rings are not offset.

To reproduce the escaped features, we construct a nonsingular Frank-Pryce model by introducing an escape angle ϵ which is 90° everywhere except near the escaped region (Fig. 8):

$$(n_r, n_\theta, n_\phi) = (\cos\epsilon, \cos\Omega\sin\epsilon, \sin\Omega\sin\epsilon). \tag{4}$$

To date, there is no solution for the functional form of ϵ; however, BZ proposed a model with a discrete disclination core where

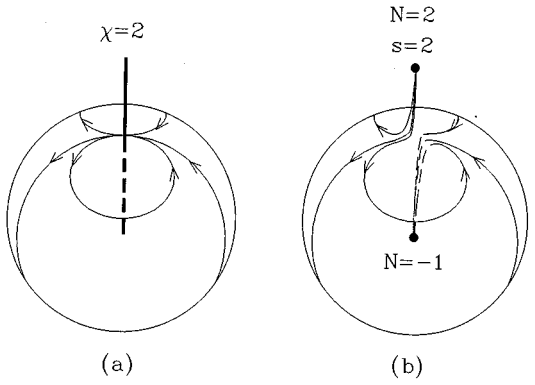

FIG. 9. Defects in the Frank-Pryce model. Lines are tangent to the director field and given an arbitrary direction toward the bulk defect. (a) The unescaped model has $\chi=2$ defect line. (b) The escaped model has two point defects with charges shown. The lines in (b) near the axis should actually spiral around the axis.

$$\epsilon = \begin{cases} 2\arctan[(\rho/r_2)^2] & \text{if } \rho < r_2 \\ 90° & \text{if } \rho > r_2. \end{cases} \tag{5}$$

At $\rho=r_2$ these solutions are both equal to 90°, but $\partial\epsilon/\partial\rho$ is discontinuous. Unfortunately, our simulations of the core are not sensitive enough to distinguish between various functional forms of ϵ, so to bring out the general features of escape we used the simpler function

$$\epsilon = \arctan[(\rho/r_2)^2], \tag{6}$$

which avoids the discontinuity in $\partial\epsilon/\partial\rho$. Otherwise, by suitably adjusting r_2, the two models can be made very similar. Photographs of the escaped Frank-Pryce structure, and the corresponding simulations, are shown in Fig. 7. Comparing the actual photograph with the simulation, it is clear that our droplets are escaped.

Although the radial line defect in the original Frank-Pryce model is removed by escaping the director to the radial direction, there are still two point defects remaining—one at the center and the other on the surface [19]. Figure 9 shows both the nonescaped and escaped Frank-Pryce structures and the defects associated with them. If we take the director to be a vector as shown, the central defect has volume charge $N=-1$, while the surface defect has a volume charge $N=2$ and a surface charge $s=2$. Below, we will show how these defects can evolve continuously from the Frank-Pryce to the twisted bipolar structure.

BZ predicted that the diametrical defect ($s=1$) structure is most stable, but we have not observed that structure in our high-chirality samples. Nor have we observed the double radial defect structure ($s=\frac{1}{2}$ and $\frac{3}{2}$). The disagreement between the theoretical prediction and the experimental results may arise from several factors: different elastic constants, finite surface anchoring, neglected higher-order elastic deformations, and escaped disclination lines. BZ discussed the effects of the first three factors, and found that they should not change the relative sizes of the free energies of the line-defect structures. If the directors in the radial and diametrical defect structures are allowed to escape, however, BZ found

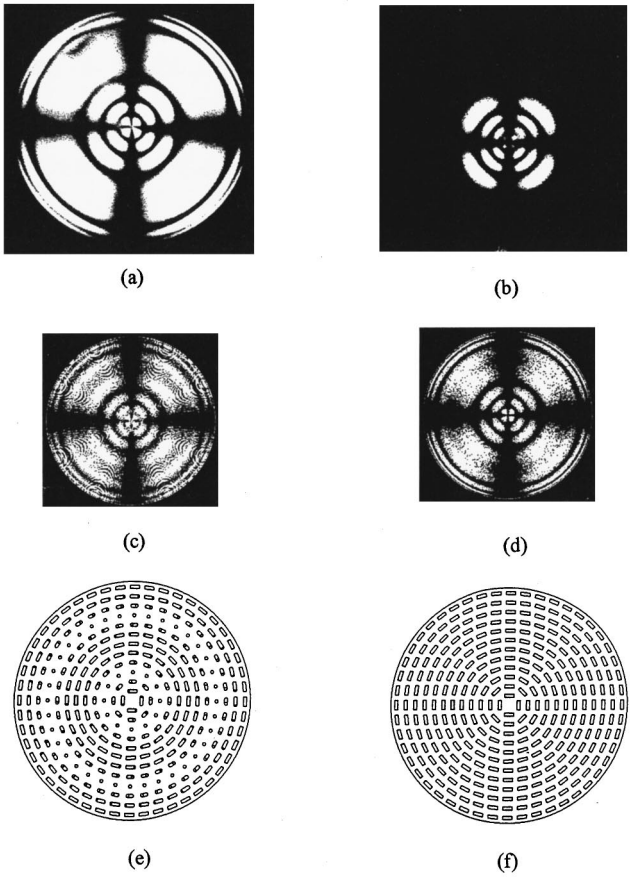

FIG. 10. (a) Picture of the chiral nematic drop with $P \ll R$. (b) Nonchiral nematic drop with perpendicular surface anchoring. (c) and (d) Simulations of (a) and (b), respectively. (e) Frank-Pryce model used for simulation in (c); cylinders represent prolate refractive index ellipsoids. (f) Radial model used for simulation in (d); refractive index ellipsoids are oblate with axes along radii of drop.

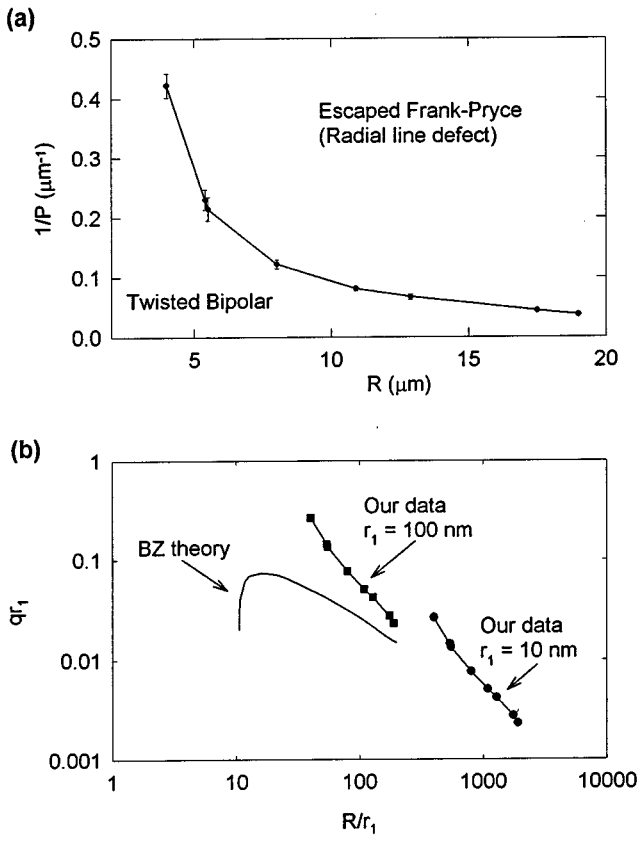

FIG. 11. (a) Phase stability diagram of chiral nematic droplets in the $1/P$ vs R plane; the error flags show the range of coexistence of the two structures. (b) Comparison of theoretical and experimental phase diagrams in the $qr_1 - R/r_1$ plane, where r_1 is the radius of the defect core.

that the escaped radial defect structure may, under certain conditions, be more stable than the escaped diametrical defect structure.

C. Very high chirality ($P \ll R$)

A very high-chirality droplet ($P = 0.82\ \mu$m, $R = 35\ \mu$m), viewed between crossed polarizers, is shown in Fig. 10(a). The appearance of this droplet is very similar to that of a nematic droplet with radial director, shown in Fig. 10(b). Nevertheless, it is impossible for a very highly chiral nematic droplet with parallel surface anchoring to have a radial structure.

Figure 10(c) shows the simulation of Fig. 10(a) from the Frank-Pryce model with $P \leqslant R$. The agreement is quite reasonable. The similarity between Figs. 10(a) and 10(b) can be understood using an ''average birefringence'' model. In the Frank-Pryce structure with high chirality, the director, and therefore the refractive index ellipsoid, lies perpendicular to and rotates uniformly about the radial pitch axis. Because the pitch is of the order of a wavelength of light in the liquid crystal, we may take the *effective* refractive index ellipsoid to be just the *actual* refractive index ellipsoid averaged over a pitch distance. For light polarized in the radial direction, the extraordinary average refractive index becomes the ordinary index: $n_{e,\mathrm{ave}} = n_o$. For light polarized perpendicular to the radius, however, the ordinary average index $n_{o,\mathrm{ave}}$ is the average over a pitch length of the projection of the extraordinary index $n_{e,\mathrm{eff}}$ on the polarization direction: $n_{o,\mathrm{ave}} = \langle n_{e,\mathrm{eff}} \rangle$. The effective index is given by [20]

$$n_{e,\mathrm{eff}} = \frac{n_o n_e}{\sqrt{n_o^2 \sin^2\theta + n_e^2 \cos^2\theta}}, \tag{7}$$

where θ is the tilt of the director from a meridional plane. Assuming $n_e - n_o$ is small, and averaging over a pitch,

$$n_{o,\mathrm{ave}} \approx n_o [1 + (n_e^2 - n_o^2)/4n_e^2], \tag{8}$$

and so the averaged birefringence is

$$\Delta n_{\mathrm{ave}} = n_{e,\mathrm{ave}} - n_{o,\mathrm{ave}} = -n_o \left(\frac{n_e^2 - n_o^2}{4n_e^2} \right). \tag{9}$$

In our chiral mixture, $n_e - n_o$ is about 10% of the average index of refraction, so that $\Delta n_{\mathrm{ave}} \approx 43\%$ of n with the opposite sign. We therefore construct an averaged director field where the director is parallel to the ''averaged optical axis,'' which is the same as the pitch axis. This averaged director

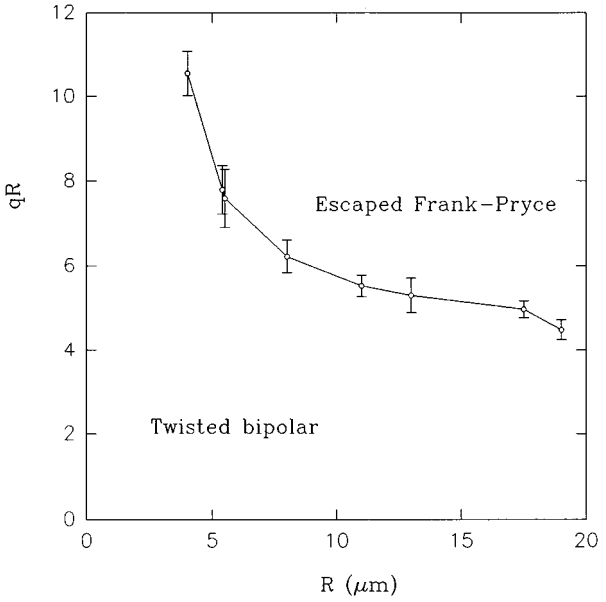

FIG. 12. Phase stability diagram in the $R/P-R$ plane. Error flags shows the region where droplets may be either Frank-Pryce or bipolar.

field is radial everywhere with birefringence Δn_{ave} and perpendicular boundary conditions as shown in Fig. 10(f).

Figures 10(c)–10(d) show simulations from the Frank-Pryce model and the average-index radial model, respectively. Overall, the two pictures are very similar; however, due to calculation errors caused by the large number of steps required for any chiral model, the two simulations may differ in detail.

D. Phase stability diagrams

For each chirality, the droplet radius at which the transition between the two structures occurs was determined by measuring the sizes of the smallest Frank-Pryce droplet and the largest twisted bipolar droplet. A phase stability diagram of the chiral nematic droplets with various chiralities and radii is displayed in Fig. 11(a) as the chirality $1/P$ versus the radius R. The size of the error flags in Fig. 11(a) gives the coexistence range of the two structures.

A comparison of our experimental data to the BZ theoretical results is shown in Fig. 11(b). In the theoretical diagram, the chirality and radius are scaled by the point defect core radius r_1. Although r_1 is not known, we scaled our data with $r_1=10$ and 100 nm for comparison with the theory. It can be seen that the chirality decreases as the radius increases for both the theoretical and the experimental curves, but the two curves cannot be fit to each other for any value of r_1. At large R, the theoretical phase diagram is similar to $qR=\mathrm{const}$ [14]. We test this possibility for our own data in Fig. 12, where qR is plotted versus R. We can see that qR does not vary much for large droplets but increases dramatically as R becomes smaller than a few micrometers.

If the surface anchoring is perfect and the core energies of the point defects are negligible (since the core radius $r_1 \ll R$), then the radius-to-pitch ratio R/P should be the only parameter to control the structures of the droplets, and qR at the transition should be independent of droplet size. We therefore propose that the increase of qR in Fig. 12 as the radius decreases is an indication that the surface anchoring is no longer perfect, i.e., the surface extrapolation length ξ is no longer much less than R. Since the rise in qR takes place when $R \approx 5\ \mu$m, we can take that length as an estimate of ξ. This relaxation of perfect surface anchoring may also be a reason for the discrepancy between the theoretical and experimental curves in Fig. 11(b).

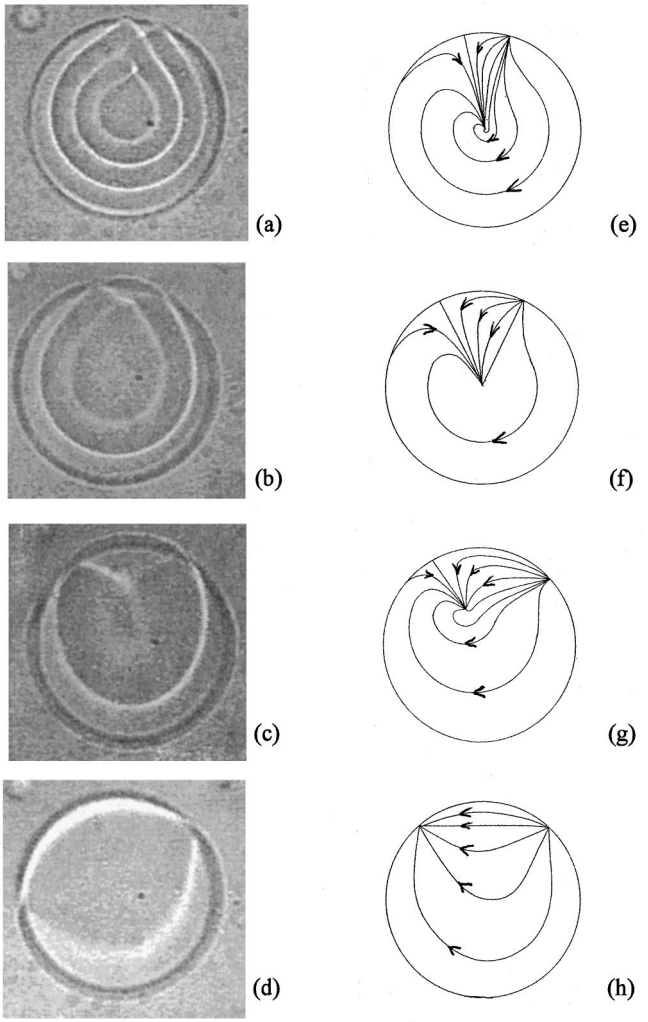

FIG. 13. Details of the bipolar–Frank-Pryce transition as the chirality decreases. (a) Surface defect splits into two surface defects. (b) Two surface defects move apart, and the number of fringes becomes smaller. (c) Central defect moves toward one surface defect and merges in (d). (e)–(h) Models for stages in (a)–(d). (e) Original $N=2$, $s=2$ surface defect splits into two $N=1$, $s=1$ surface defects. (f)–(g) New surface defects move apart. (h) Central $N=-1$ bulk defect combines with surface defect to produce an $N=0$, $s=1$ surface defect. At all stages of the process, $\Sigma N=1$ and $\Sigma s=2$.

E. Mapping the structural transition

As the ratio R/P is reduced, a structural transition takes place from the Frank-Pryce to the bipolar structure. It is interesting to see the details of this transition, and, in particular, to ask whether such a transition can take place continuously. Experimentally we found that the transition may

happen through different intermediate states, some of which appear quite symmetrical and others which look quite chaotic.

To study the transition process under conditions of slowly varying pitch, we used a liquid crystal mixture (ZLI-2806–D-112–D-13) whose pitch could be continuously adjusted by changing the temperature as shown in Fig. 1(b). Among the many possibilities for such a transition, we show one interesting one which was captured on video. Similar transition processes were also observed in newly made samples of the ZLI-4788-000–S-811 mixture while droplets were relaxing to their equilibrium states.

Figure 13 shows pictures of a chiral nematic droplet taken during the transition from the Frank-Pryce to the twisted bipolar structure as the chirality decreases. No polarizers were used; the bright lines are from regions where the refractive index is changing rapidly. Also shown is our interpretation of the process. Figure 9(b) has already shown the bulk and surface defects in the escaped Frank-Pryce structure. Figure 13(a) shows the surface defect split into two surface defects, which then move apart in Figs. 13(b) and 13(c). In Fig. 13(d), one of the surface defects combines with the bulk defect to form the bipolar structure.

Our interpretation of this process is shown in Figs. 13(e)–13(h); assignment of topological charges follows the rules of Volovik and Lavrentovich [19]. Giving the director a direction toward the bulk defect, the Frank-Pryce structure starts out with a bulk defect ($N=-1$) and a single surface defect ($N=2$, $s=2$). During the transition, the surface defect splits into two surface defects, one a half-hedgehog and the other half-hyperbolic. Despite their differences, these defects have the same surface charges $s=1$ and volume charge $N=1$. The half-hyperbolic surface defect then combines with the bulk defect to produce a new $N=0$, $s=1$ surface defect along with the remaining $N=1$, $s=1$ surface defect. Although these defects look the same, the difference in their volume charges is a result of the assigned director direction and is somewhat arbitrary. Note, however, that at all times during the transition the rules regarding the sum of topological charges on a sphere are obeyed—namely, the total volume charge is 1 and the total surface charge is 2.

IV. CONCLUSIONS

Our results agree generally with those of Bezic and Zumer [14], but differences in detail are evident. For low chirality we confirmed that chirality causes the twisted bipolar structure rather than the predicted nematic bipolar structure. The inclusion of twist in the BZ bipolar model will certainly affect their phase stability diagram. For high chirality, we confirm that the structure is Frank-Pryce and not the diametrical model, and that the line defect is in fact escaped, a situation which BZ also considered. Their calculations were difficult, however, and they could only suggest that the radial structure may have the lower energy. In light of the above considerations, it does not seem surprising that our experimental and their theoretical phase diagrams agree only qualitatively.

Finally, we have examined in detail the process where the Frank-Pryce structure changes to the escaped bipolar structure. This transition has yet to be addressed theoretically and, indeed, may take place in several ways. Further work on this and other such transitions should prove interesting.

[1] *Liquid Crystals in Complex Geometries*, edited by G. P. Crawford and S. Zumer (Taylor and Francis, London, 1996), and references therein.

[2] P. S. Drzaic, *Liquid Crystal Dispersions* (World Scientific, Singapore, 1995).

[3] P. P. Crooker and F. Xu, in *Chiral Liquid Crystals*, edited by L. Komitov, S. T. Lagerwall, and B. Stebler (World Scientific, Singapore, in press).

[4] J. W. Doane, MRS Bull. **16**, 22 (1991).

[5] R. Ondris-Crawford, E. P. Boyko, B. G. Wagner, J. H. Erdmann, S. Zumer, and J. W. Doane, J. Appl. Phys. **69**, 6380 (1991).

[6] O. D. Lavrentovich, Zh. Eksp. Teor. Fiz. **43**, 297 (1986) [Sov. Phys. JETP **43**, 382 (1986)].

[7] P. S. Drzaic, Mol. Cryst. Liq. Cryst. **154**, 289 (1988).

[8] F. Xu, H.-S. Kitzerow, and P. P. Crooker, Phys. Rev. E **49**, 3061 (1994).

[9] F. Xu, H.-S. Kitzerow, and P. P. Crooker, Phys. Rev. A **46**, 6535 (1992).

[10] J. H. Erdmann, S. Zumer, and J. W. Doane, Phys. Rev. Lett. **64**, 1907 (1990).

[11] H.-S. Kitzerow, Liq. Cryst. **16**, 1 (1994).

[12] M. Kurik and O. D. Lavrentovich, Pis'ma Zh. Eksp. Teor. Fiz. **35**, 362 (1982) [JETP Lett. **35**, 444 (1982)].

[13] P. P. Crooker and D. K. Yang, Appl. Phys. Lett. **57**, 2529 (1990).

[14] J. Bezic and S. Zumer, Liq. Cryst. **11**, 593 (1992).

[15] J. Bajc, J. Bezic, and S. Zumer, Phys. Rev. E **51**, 2176 (1995).

[16] G. Heppke, D. Lötzsch, and F. Oestreicher, Z. Naturforsch. Teil A **41**, 1214 (1986); G. Heppke, D. Lötzsch, and F. Oestreicher, *ibid.* **42**, 279 (1987).

[17] A. Feldman, P. P. Crooker, and L. M. Goh, Phys. Rev. A **35**, 842 (1987).

[18] H.-S. Kitzerow and P. P. Crooker, Liq. Cryst. **13**, 31 (1993).

[19] The strength of a topological charge is arrived at by mapping the director orientation from a surface surrounding the defect onto a *director space* containing all possible director orientations. The number of times the director space is covered determines the strength. For a description of both surface and volume charges, see G. E. Volovik and O. D. Lavrentovich, Zh. Eksp. Teor. Fiz. **85** 1997 (1983). [Sov. Phys. JETP **58**, 1159 (1983)], and references therein.

[20] B. E. A. Saleh and M. C. Teich, *Fundamentals of Photonics* (Wiley, New York, 1991), p. 218.